UC Riverside

UC Riverside Previously Published Works

Title

Mechanics of Porcine Heart Valves Strut Chordae Tendineae Investigated as a Leaflet-Chordae-Papillary Muscle Entity.

Permalink

Journal

Authors

Ross, Colton
Laurence, Devin
Hsu, Ming-Chen
et al.

Publication Date

DOI

Mechanics of porcine heart valves' strut chordae tendineae investigated as a leaflet-chordae-papillary muscle entity

Colton J. Ross[1], **Devin W. Laurence**[1], **Ming-Chen Hsu**[2], **Ryan Baumwart**[3], **Yan D. Zhao**[4], **Arshid Mir**[5], **Harold M. Burkhart**[6], **Gerhard A. Holzapfel**[7,8], **Yi Wu**[1], **Chung-Hao Lee**[1,9]

[1]Biomechanics and Biomaterial Design Laboratory School of Aerospace and Mechanical Engineering The University of Oklahoma Norman, OK 73019, USA

[2]Department of Mechanical Engineering Iowa State University Ames, IA 50011, USA

[3]Center for Veterinary Health Sciences Oklahoma State University Stillwater, OK 74078, USA

[4]Department of Biostatistics and Epidemiology, The University of Oklahoma Health Sciences Center Oklahoma City, OK 73104, USA

[5]Department of Pediatric Cardiology , The University of Oklahoma Health Sciences Center Oklahoma City, OK 73104, USA

[6]Department of Surgery, The University of Oklahoma Health Sciences Center Oklahoma City, OK 73104, USA

[7]Institute of Biomechanics Graz University of Technology Graz, Austria

[8]Department of Structural Engineering Norwegian University of Science and Technology (NTNU) Trondheim, Norway

[9]Institute for Biomedical Engineering, Science and Technology The University of Oklahoma Norman, OK 73019, USA

Abstract

Proper blood flow through the atrioventricular heart valves relies on the holistic function of the valve and subvalvular structures, and failure of any component can lead to life-threatening heart disease. A comprehension of the mechanical characteristics of the healthy valve components is necessary for the refinement of heart valve computational models. In previous studies, the chordae tendineae have been mechanically characterized as *individual* structures, usually in a clamping-based approach, which may not accurately reflect the *in vivo* chordal interactions with the leaflet and papillary muscles insertion regions. In this study, we performed uniaxial mechanical testing of strut chordae tendineae of the atrioventricular heart valves under a unique tine-based leaflet-chordae-papillary muscle testing to observe the chordae mechanics with preserved subvalvular component interactions. Results of this study provided insight to the disparity of chordae tissue

For correspondence: Chung-Hao Lee, Ph.D., Assistant Professor, School of Aerospace and Mechanical Engineering, The University of Oklahoma, 865 Asp Ave., Felgar Hall Rm. 219C, Norman OK 73019-3609, U.S.A., ch.lee@ou.edu; Tel: +1-405-325-4842.

stress-stretch responses between the mitral valve (MV) and the tricuspid valve (TV) under their respective emulated physiological loading. Specifically, strut chordae tendineae of the MV anterior leaflet had peak stretches of 1.09–1.16, while peak stretches of 1.08–1.11 were found for the TV anterior leaflet strut chordae. Constitutive parameters were also derived for the chordae tissue specimens using an Ogden model, which is useful for computational model refinement. Results of this study are beneficial to the eventual improvement of treatment methods for valvular disease.

1. Introduction

Unidirectional blood flow through the heart chambers is regulated by the four cardiac valves: two semilunar valves, and two atrioventricular heart valves (AHVs)—the mitral valve (MV) and tricuspid valve (TV). The MV is composed of two leaflets designated by their anatomical location as the anterior leaflet (MVAL) and the posterior leaflet (MVPL), whereas the TV contains three leaflets—the anterior leaflet (TVAL), the posterior leaflet (TVPL), and the septal leaflet (TVSL). For the AHVs, blood flow direction is facilitated by the collagenous tissue leaflets that are supported in their function by the chordae tendineae (CT) that connect the valve leaflets to the papillary muscles of the ventricular wall. The chordae tendineae provide necessary supporting forces to prevent leaflet prolapse into the atria during systole.[14] The chordae tendineae can be classified based on their insertion point to the AHV leaflet: *strut* chordae as those two thickest segments attaching to the MVAL's and TVAL's rough zones, *marginal* chordae as those attaching to the leaflet's free edge, and *basal* chordae as those attaching near the leaflet's base.

When the chordae rupture, prolapse of the leaflet into the atria leads to valvular regurgitation, resulting in an increased workload of the heart and worsened prognosis.[33] Several surgical techniques have been employed to treat chordae rupture, including chordal shortening, chordal transposition, and chordal replacement—each with their own limitations. For example, chordal shortening may not always yield the optimal treatment results.[28] Chordal transposition provides a desirable mid-term freedom from reoperation, but still requires further investigations to confirm its effectiveness.[29] Moreover, chordal replacement utilizes expanded polytetrafluoroethylene (ePTFE) to replace the chordae tendineae. This technique is advantageous as it is minimally invasive with an excellent recurrence rate of 1.4% at 3.5 years;[20] however, in the long-term, recurrence may be caused by excessive elongation and rupture of the native chordae tendineae.[4,32] Additionally, the elastic moduli of ePTFE sutures are significantly larger than those of native CTs that may potentially lead to the recurrent prolapse.[3] Improvement of surgical therapeutics would rely on a better understanding of the tissue mechanics of native chordae tendineae.

Studies in AHV biomechanical modeling have utilized the experimentally-characterized valve leaflets' mechanical properties.[16,22] Effort has also been devoted to incorporating the chordae tendineae into these computational models using experimental data in the literature.

The majority of those experimental CT characterizations considered the strut CT specifically, since the strut chordae tendineae has been shown to experience greater *in vivo* loading than the other chordae tendineae categories.[18] These experimental studies[21,22,24,34] have been primarily focused on characterizing *individual* CT segments, rather than considering a leaflet-chordae-papillary muscle entity testing configuration which preserves interactions between the chordae and the leaflet as well as between the chordae and the papillary muscles (PMs). A recent study by Gunning and Murphy[8] moved towards this modified experimental setup, in which a customized clamping method was developed with a leaflet-CT-PM entity. Nonetheless, this clamping method did not adequately allow deformations of the leaflet insertion or papillary muscle attachment.

To further advance our knowledge in the mechanical behavior of AHV chordae tendineae, the objective of this study is to characterize the strut chordae by means of a leaflet-CT-PM entity. This characterization was performed using a tine-based tissue mounting that preserves the interactions between the CT and the valve leaflet, and between the chordae and the papillary muscles. The data reported from this study provide a new insight into the biomechanical role of the chordae tendineae in the AHV function, where mechanical interactions among the CT, valve leaflets, and papillary muscles are considered together. Such improved understanding of AHV strut CT tissue mechanics could also help with the development of AHV computational models to guide surgical treatment of chordae rupture-induced valvular heart disease.

2. Methods

2.1 Tissue Preparation

Twelve healthy porcine hearts (80–140 kg, 1–1.5 years of age) were obtained from a local USDA approved abattoir (Country Home Meat Co., OK), cleaned of blood clots, and frozen for prolonged storage.[30] Within 2 days of tissue acquisition, hearts were thawed and the chordae tendineae were excised from each of the AHVs while preserving the papillary muscles and leaflet points of attachment (Fig. 1a).

In this study, strut CT of the MVAL and TVAL were selected for mechanical testing because they have been previously shown as the primary load-bearing CT during systolic closure of the AHV.[18] Strut CT specimens were retrieved from each side of both the MVAL and TVAL apices, resulting in two CT groups per leaflet. These samples were labeled with respect to their location: LG–left chordae group; RG–right chordae group. For the MVAL, the LG is adjacent to the posteromedial commissure and the RG is adjacent to the anterolateral commissure (Fig. 1b). For the TVAL, the LG and the RG are adjacent to the anteroseptal and anteroposterior commissures, respectively. Tissue specimens were then stored in phosphate buffered saline solution in a refrigerated environment at 4 °C until later mechanical testing within 12 hours after dissection.[27] Measurements of the chordae thickness D at three points about the center of the CT, which was used in the tissue stress calculation, were recorded with an AmScope microscope at 4X magnification (United Scope LLC, CA) both before and after uniaxial mechanical testing (Fig. 1c).

2.2 Uniaxial Testing

Uniaxial mechanical testing was performed using the BioTester mechanical testing system (CellScale Biomaterials Testing, Waterloo, Canada), equipped with 1.5N capacity load cells. Samples were mounted by five-tined BioRakes, anchoring the papillary muscles and AHT leaflet to the BioTester system and allowing in-plane stretching of the CT, leaflet, and papillary muscles (Fig. 1d). Approximately 5–7 fiducial markers, depending on the specimen's dimension, were placed on the CT segment using a surgical pen for subsequent marker coordinate tracking, as described in Section 2.3.

A two-step force-controlled uniaxial testing protocol was employed for characterizing the CT tissues (Fig. 1e). Briefly, the MVAL/TVAL strut chordae tissues were first subjected to a *preconditioning* step of eight loading/unloading cycles using a linear ramp to the targeted force F_{max} with a rate of 4.42 N/min to restore the tissues to *in vivo* condition.[2] A maximum force of 1.4 N for the MVAL CT tissue samples was chosen for its similarity to the approximate 1.5 N force that the MVAL strut chordae experience under physiological loading, as observed in a previous *in vitro* experiment.[12] Similarly, a maximum force of 1.2 N was used for the TVAL chordae tissues, as the TV is subjected to a lower pressure gradient than the MV counterpart.[13] The loading rate of 4.42 N/min was used according to the equivalent loading rates from previous displacement-based CT mechanical characterizations, such as 3–5 mm/min in the previous *in vitro* studies.[21,22] After preconditioning, the mechanical testing step was carried out with another eight loading-unloading cycles (Fig. 1e).

2.3 Tissue Stretch and Stress Calculations

Using the digital image correlation (DIC) module in the LabJoy software of the BioTester, the coordinates (x_i, y_i) of the center of the fiducial marker i were tracked (Fig. 1d), and, then, the marker's x- and y-displacements (u_i, v_i) between any two loading states were computed. The tissue stretch of the i-th CT segment between node i and node $i+1$ was determined using a one-dimensional two-node linear finite element

$$\lambda_i = \frac{2}{l_i}\begin{bmatrix} -\frac{1}{2} & \frac{1}{2} \end{bmatrix}\begin{bmatrix} d_i \\ d_{i+1} \end{bmatrix} + 1, \tag{1}$$

where $l_i = \sqrt{(x_{i+1} - x_i)^2 + (y_{i+1} - y_i)^2}$ is the segment length, and d_i and d_{i+1} are the displacements of nodes i and $i+1$, respectively, along the axial direction of the i-th segment, i.e.,

$$d_i = u_i\cos\theta + v_i\sin\theta, \;\; d_{i+1} = u_{i+1}\cos\theta + v_{i+1}\sin\theta, \;\; \tan\theta = \frac{y_2 - y_1}{x_2 - x_1}. \tag{2}$$

Each stretch λ of the CT tissue was obtained by averaging the stretch values of all the chordae tendinea segments, i.e., $\lambda = \frac{1}{m}\sum_{i=1}^{m} \lambda_i$ where m is the number of segments of each CT tissue specimen.

Since a uniform strain field was an inherent consequence of the above two-node linear finite element formulation, to further examine the *tissue stretch distribution* across the CT specimen, we also performed a cubic spline space curve fit to the fiducial markers using the cscvn built-in function in MATLAB (MathWorks, MA). Following a similar procedure in the previous study on dynamics of the mitral valve annulus,[5] the spline-based stretch calculation for each CT tissue was made. Next, the Cauchy stress σ of the CT tissue was calculated by

$$\sigma = \left[\frac{F}{A_0}\right] \lambda \, , \tag{3}$$

where F is the force of the load cell reading, and $A_0 = \pi D^2/4$ is the undeformed area of the CT, assuming an idealized, circular cross-section with the measured thickness D.

2.4 Constitutive Modeling of the CT Mechanics

The CT tissues were idealized as a nonlinear, isotropic, incompressible solid and modeled by using the one-term Ogden hyperelastic constitutive model (p=1)[19]

$$\sigma = \mu\left(\lambda^\alpha - \lambda^{-\frac{\alpha}{2}}\right) , \tag{4}$$

where μ and α are model parameters, which were estimated by nonlinear least-squares fitting to the tissue stress-stretch data using an in-house differential evolution optimization program with a residual error tolerance of 10^{-10} as the convergence criteria.[31] The normalized root-mean-square deviation (NRMSD) was computed as a metric to assess the nonlinear fit of Eq. (4) to the chordae tendineae's mechanical data. Herein, the NRMSD, defined as the square root of the average of squared errors, was normalized with respect to the maximum stress value.

2.5 Statistical Analysis

Physical quantities, such as the measured CT thickness and the quantified tissue stress and stretch, were reported as mean ± standard error of the mean (SEM). Note that the *peak stretch* $\lambda^{(0\text{-}2)}$ quantified in Section 2.3 is defined as the stretch at peak loading state Ω_2 with respect to the tissue mounting configuration Ω_0. Previous studies have reported a difference in the tissue's stretch responses between preconditioning and the applied loading.[9] Thus, we further decomposed the peak stretch into the following two components for statistical analyses: (i) the *preconditioning stretch* $\lambda^{(0\text{-}1)}$, defined as the stretch at the end of the preconditioning Ω_1, and (ii) the *stretch* $\lambda^{(1\text{-}2)}$ associated with the peak tension with respect to Ω_0, such that $\lambda^{(0\text{-}2)} = \lambda^{(1\text{-}2)}\lambda^{(0\text{-}1)}$. The stretch was used in the constitutive modeling described in Section 2.4, and the three components of the tissue stretch were then considered in the subsequent statistical analyses.

Residual plots were developed for each of the above-mentioned parameters associated with the CT tissues to examine the data normality and constant variance (see Figs. S1–S4 in the Supplementary Material section). Significant departure from normality resulted in the use of the non-parametric Wilcoxon rank-sum test for the statistical analyses with the null

hypothesis that the means of the two compared groups are identical. Statistical analyses were performed using SAS 9.4 (SAS Institute Inc., NC), and the significance was defined as *significant* (p<0.05) and *non-significant* (p 0.05).

3. Results

3.1 Mechanical Results and CT Thickness

The Cauchy stress-stretch responses of the CT tissues followed a nonlinear, exponential trend (Fig. 2), with the stress values at F_{max} reported as follows: 1.59 ± 0.16 MPa (MVAL-LG), 1.04 ± 0.08 MPa (MVAL-RG), 2.71 ± 0.10 MPa (TVAL-LG), and 2.89 ± 0.01 MPa (TVAL-RG). Mechanical testing responses were further examined as the *peak* stretches $\lambda^{(0-2)}$, *preconditioning* stretches $\lambda^{(0-1)}$, and the stretches $\lambda^{(1-2)}$.

The peak stretches were (Fig. 3a): 1.09 ± 0.02 (MVAL-LG), 1.16 ± 0.02 (MVAL-RG), 1.08 ± 0.02 (TVAL-LG), and 1.11 ± 0.01 (TVAL-RG). Statistically significant difference in the median was found between the two MVAL CT tissue groups (p=0.046), while no significant difference in the median was observed between the TVAL CT tissue groups (p=0.112). Moreover, the preconditioning stretches were 1.07 ± 0.02 for the MVAL-LG, 1.14 ± 0.02 for the MVAL-RG, 1.06 ± 0.02 for the TVAL-LG, and 1.08 ± 0.01 for the TVAL-RG (Fig. 3b). Significant difference in the median was found between the two MVAL CT tissue groups (p=0.03), but there was no significant difference in the median between the TVAL tissue groups (p=0.26). Furthermore, the stretches for various CT tissue groups were reported as follows (Fig. 3c): 1.03 ± 0.01 (MVAL-LG), 1.02 ± 0.01 (MVAL-RG), 1.02 ± 0.01 (TVAL-LG), and TVAL-RG, 1.03 ± 0.01 (TVAL-RG). No significant differences in the median were found in the stretch between the MVAL CT tissue groups (p=0.507) or between the TVAL tissue groups (p=0.371).

Finally, the measured CT thicknesses were 1.08 ± 0.08 mm for the MVAL-LG, 1.32 ± 0.07 mm for the MVAL-RG, 0.76 ± 0.09 mm for the TVAL-LG, and 0.74 ± 0.07 mm for the TVAL-RG (Fig. 3d). Comparing the two tissue groups of each AHV leaflet, statistically significant difference in the median was found only for the MVAL groups (p=0.040), but not for the TVAL groups (p=0.931).

3.2 Constitutive Modelling Results

The estimated Ogden model parameters for each tissue specimen are summarized in Table 1, with representative fitting results demonstrated in Figure 4a–b. In general, the Ogden model was able to capture the nonlinear Cauchy stress-stretch behavior of the strut CT tissues, with parameter μ: 86.2 ± 46.7 kPa (MVAL-LG), 29.9 ± 12.0 kPa (MVAL-RG), 494.8 ± 131.8 kPa (TVAL-LG), and 457.2 ± 304.8 kPa (TVAL-RG), and parameter α: 200.6 ± 16.9 (MVAL-LG), 271.3 ± 16.4 (MVAL-RG), 132.8 ± 13.0 (TVAL-LG), and 134.8 ± 16.3 (TVAL-RG).

4. Discussion

4.1 Overall Findings and Comparisons to Existing Literature

First, we found that the MVAL strut CT were ~45% larger than the TVAL counterparts (MVAL: *D*=1.20 ± 0.06 mm, TVAL: *D*=0.75 ± 0.05 mm; Fig. 3d), which consistently

reflects that a higher pressure gradient is present in the mitral valve residing in the left side of the heart. We also noticed for the MVAL that the right chordae group was generally thicker (MVAL-LG: D=1.08 ± 0.08 mm, MVAL-RG: D=1.32 ± 0.07 mm) and more extensible (MVAL-LG: $\lambda^{(0\text{-}2)}$=1.10 ± 0.02, MVAL-RG: $\lambda^{(0\text{-}2)}$=1.16 ± 0.02) in comparison to the left chordae group (Fig. 3a–c), whereas this trend was not observed in the strut chordae of the TVAL. Furthermore, the mechanical responses of the strut CT tissues followed an exponential, nonlinearly elastic trend expected of collagenous soft tissues (Fig. 2). As for the constitutive modeling, the Ogden model was successful in capturing the nonlinear stress-stretch responses of the tested strut CT (Fig. 3 and Table 1). Overall, the TVAL strut chordae had a larger μ parameter (476.0 ± 162.4 kPa) compared to the MVAL counterparts (58.0 ± 24.3 kPa), indicating a higher stress transition in the stress-stretch curve (Fig. 2 and Fig. 3). In contrast, parameter α was less varied between the MVAL and TVAL strut CT (i.e., MVAL: 235.9 ± 13.7, TVAL: 133.8 ± 10.2).

As opposed to other testing schemes, such as using individual segments[17,21,24,34] or using leaflet-chordae-papillary muscle entities[8] (where the PM and leaflet deformations are restricted as depicted in Figure 5b), there are some differences in the quantified CT mechanics when our leaflet-chordae-papillary muscle entity testing method (Fig. 5a) was used. In general, the stretch was smaller in this study than that reported in the previous porcine and ovine studies on characterizing *individual* CT (Table 2). However, when comparing to human individual CT testing results, our stretch values were more comparable to those found in Prot *et al.* (2010).[22]

Comparing the constitutive parameters, our estimated parameter values are within a similar range to those reported in the previous studies (Table 1).[21,34] Note that in our study we provided constitutive parameters for each CT specimen, whereas Pokutta-Paskaleva *et al.* (2019)[21] and Zuo *et al.* (2016)[34] reported constitutive parameters for the *averaged* stress-stretch responses.

4.2 Potential Advantages of the Proposed CT-Entity Testing Method

Results of this study provide some new insight into the interrelationship of the CT tissue mechanics with the connected papillary muscle and the valve leaflet. The presented method of testing the chordae tendineae offers several potential advantages. For example, this leaflet-CT-PM entity testing method could be used to understand the varying stretches in each segment of the CT (e.g., our results presented in Figures 6–7) and to examine the distribution of mechanical loading to the three subvalvular components (i.e., among chordae tendineae, leaflet, and papillary muscles). Moreover, collagen fiber microstructural imaging techniques, such as the polarized spatial frequency domain imaging (pSFDI),[11] could be integrated with this CT-entity testing scheme to quantify the collagen fiber reorientations of the chordae insertion regions. Our group is currently performing pilot investigations to explore such potential advantages of our CT-entity testing method. Our preliminary results, as shown in Figure 5c, summarize the quantified reorientations and realignment of the collagen fiber networks for the CT-leaflet insertion at two representative loading states. These results from this internal pilot study demonstrate that for the MVAL CT-leaflet insertion region, collagen fibers become better aligned under an increased uniaxial load, as

evidenced by the increase in the degree of optical anisotropy. A brief description about the pSFDI imaging procedure adopted in this pilot study is provided in the Appendix. For more details about the pSFDI-based collagen fiber imaging technique and the corresponding data analyses, the reader is referred to our recent publication[11] and the previous work by Goth *et al.* (2019).[7]

We have used the presented method to perform some preliminary analyses of the deformations of both the valve leaflet and the PM segments in our leaflet-chordae-papillary muscle entity testing. Specifically, we used a surgical pen to construct a 2×2 marker array on each of the leaflet and PM regions, and then employed a four-node single finite element to calculate the tissue strains based on marker coordinates determined by the digital image correlation method.[1,10] For the leaflet segment, the stretches were 1.09 ± 0.07 (MVAL, n=3), and 1.06 ± 0.01 (TVAL, n=5). As for the papillary muscles, the stretches were 1.03 ± 0.07 (MVAL, n=3) and 1.06 ± 0.01 (TVAL, n=5). Comparing to the CT segment stretches, the papillary muscles and leaflet stretches were generally higher than that of the CT segment, suggesting the essential interactions among the AHV leaflets, the papillary muscles, and the chordae tendinea segment. Further investigations with a larger sample size would be useful to confirm the observed trends.

Another uniqueness of our leaflet-chordae-papillary muscle entity testing setup and spline-based tissue deformation calculation was that the variations in the tissue stretch across the CT specimen were, *for the first time*, quantified (Fig. 6). From these novel results, we observed that the largest stretch occurred primarily near the leaflet insertion. This observation was further confirmed when the stretches were averaged across four quarter-segments of the CT domain, where the leaflet insertion (1Q) exhibited the highest stretch (Fig. 7). Previous failure analyses of the CT found the leaflet insertion region to be the most rupture-vulnerable area, which is consistent with our observed trend.[25] This is also consistent with where chordae typically rupture in the human mitral valves.

4.3 Study Limitations and Future Extensions

There are a few limitations in this study. First, freezing of the porcine hearts was used prior to the mechanical testing for prolonged preservation of tissues. Previous studies have found that freezing does not affect the mechanics of soft tissues, such as skin and arterial tissue,[6,30] but papillary muscles included in this study may be affected by the freezing-storage procedure, which warrants future investigations. Secondly, the testing configuration we used did not represent the three-dimensional movement of the CT structure may experience *in vivo*. It may be beneficial to perform the mechanical characterizations of the leaflet-chordae-papillary muscle entity by using a left-heart or right-heart simulator[23] to further evaluate the findings of the present study. Specifically, it would be worth to investigate how the papillary muscles interact with the ventricular attachment, along with the papillary muscles' non-uniform contractile motions, and to examine how the left-sided ventricular pathologies influence the right-sided sub-valvular components. Thirdly, the testing method proposed cannot be used to evaluate the CT rupture mechanics as the papillary muscles or leaflets would tear from their tine insertions before the CT would break. Nevertheless, the methodology presented in this study is useful for investigating the mechanics under

physiologically-representative loading, as there is no tearing of the attachments at the targeted forces. Another minor limitation is the use of the spline-based approach to quantify the tissue stretch, by which errors may be introduced during the spline-based curve smoothing/fitting process. Nonetheless, we have verified internally that minimal differences (<3%) in the calculated tissue stretches of the chordae tendineae were found between the finite element-based and splined-based methods (see Section 2.3).

The mechanical testing procedure developed in this study could be extended to analyze the previously-categorized CT of each AHV by testing as a leaflet-chordae-papillary muscle entity (e.g., basal, marginal, strut).[15,27] Another extension includes further analyses of the PM and leaflet strains during the CT testing. Analyzing the three components of the tissue stretches could also help to better understand the rupture of the chordae tendineae, which with the most common being those inserting to the central, belly region of the leaflet.[26] Additionally, the testing method presented could also be used to study *human* chordae-leaflet-papillary muscle entities. These future research efforts could lead to refinements of predictive computational models for physiological function and surgical treatments of the atrioventricular heart valves.

4.4   Conclusion

The tine-based uniaxial mechanical testing method we employed in this study is unique, because the leaflet-chordae-papillary muscle entity is kept intact during the testing. The stress-stretch responses of the AHV's chordae tendineae were analyzed as a tissue entity with papillary muscles and leaflet portion preserved to include the mechanical interactions between the CT and the leaflet as well as between the CT and the PMs. This testing methodology allows new insight to the mechanics of chordae tendineae. As compared to previous studies, we observed that the quantified tissue stretches were not uniformly distributed across the CT segments. Findings of this study suggest that preservation of the papillary muscles and leaflet points of attachment could have a direct impact on the observed mechanical properties of the strut chordae tendineae. The results of this work could be useful for the refinement of valvular disease therapeutics. For example, the CT replacement ePTFE sutures could be constructed to handle the TV physiological environment in a more desirable condition by remedying the issues of excessive elongation or rupture.

Supplementary Material

Refer to Web version on PubMed Central for supplementary material.

Acknowledgments

Appendix:

Polarized Spatial Frequency Domain Imaging (pSFDI) for Quantification of the Collagen Fiber Architecture of the Chordae-Leaflet Insertion Region

In this Appendix, we briefly discuss about the imaging method used to obtain the collagen fiber orientations of the chordae-leaflet insertion region, as described in Section 4.2. The polarized spatial frequency domain imaging (pSFDI) technique takes advantage of the polarized light-dependent birefringent properties of the collagen fibers. This birefringent property of the collagen fibers can be used in conjunction with a polarizer, a camera, and a light projector to quantify the collagen fiber orientations based on the intensity of reflected light from the fiber. The imaging is performed in the sequential order (see Figures 1–2 of Jett *et al.* (2019)[11]):

i.   Projected incident light through a polarizer at an angle $\theta_{polarizer}$ onto the tissue specimen

ii.   The incident light is reflected from the collagen fibers

iii.   The reflected light passes through a polarizer at the same $\theta_{polarizer}$ as in step (i)

iv.   The light intensity at the specific $\theta_{polarizer}$ is captured by a camera

This imaging procedure is conducted for $\theta_{polarizer}$ ranging from 0° to 180° (at an increment of 5°) to capture the intensity of the collagen fibers. Owing to the birefringent response of the collagen fiber networks, the *peak intensity* of reflected light represents the quantified collagen fiber orientation angle $\theta_{polarizer}$. In addition, the captured light intensity, say I_{out}, can be described by the following three-term Fourier series:

$$\frac{I_{out}}{\tau_{sys}} = a_0 + a_2\big[2\big(\theta_{fiber} - \theta_{polarizer}\big)\big] + a_4\big[4\big(\theta_{fiber} - \theta_{polarizer}\big)\big] \,, \tag{A5}$$

where τ_{sys} represents the non-birefringent intensities, and a_0, a_2, and a_4 are the three Fourier coefficients. Specifically, a_0 describes the mean reflected light intensity from the sample, whereas a_2 and a_4 represent the optical anisotropies arising from the sample's birefringence.

After obtaining the orientation angle of the collagen fibers, the degree of fiber alignment can be quantified through an optics-based metric – the degree of optical anisotropy (DOA):

$$DOA = \frac{a_2 + a_4}{a_0 + a_2 + a_4} \,. \tag{A6}$$

The technology also allows for investigating the collagen fiber orientation and dispersion *at varied depths* of the tissue based on the spatial frequency domain imaging (SFDI) theory. However, the preliminary result presented in this study (Fig. 5c) only contains the tissues' collagen fiber architecture through the full tissue depth. For more details about the SFDI theory, the pSFDI imaging procedures, and the corresponding data analyses, the reader is referred to Jett *et al.* (2019)[11] and Goth *et al.* (2019).[7]

References

1. Billiar KL and, Sacks MS. A method to quantify the fiber kinematics of planar tissues under biaxial stretch. J. Biomech. 30:753–756, 1997. [PubMed: 9239558]

2. Chuong C-J and, Fung Y-C. Residual Stress in Arteries. In: Frontiers in Biomechanics, Springer, 1986, pp. 117–129.

3. Cochran RP and, Kuzelman KS. Comparison of viscoelastic properties of suture versus porcine mitral valve chordae tendineae. J. Card. Surg. 6:508–513, 1991. [PubMed: 1815776]

4. Colli A, Manzan E, Rucinskas K, Janusauskas V, Zucchetta F, Zakarkait D, Aidietis A and, Gerosa G. Acute safety and efficacy of the NeoChord procedure. Interact. Cardiovasc. Thorac. Surg. 20:575–581, 2015. [PubMed: 25690455]

5. Eckert CE, Zubiate B, Vergnat M, Gorman JH, Gorman RC and, Sacks MS. In vivo dynamic deformation of the mitral valve annulus. Ann. Biomed. Eng. 37:1757–1771, 2009. [PubMed: 19585241]

6. Foutz TL, Stone EA and, Abrams CF III. Effects of freezing on mechanical properties of rat skin. Am. J. Vet. Res. 53:788–792, 1992. [PubMed: 1524309]

7. Goth W, Potter S, Allen ACB, Zoldan J, Sacks MS and, Tunnell JW. Non-destructive reflectance mapping of collagen fiber alignment in heart valve leaflets. Ann. Biomed. Eng. 47:1250–1264, 2019. [PubMed: 30783832]

8. Gunning GM and, Murphy BP. Characterisation of the fatigue life, dynamic creep and modes of damage accumulation within mitral valve chordae tendineae. Acta Biomater. 24:193–200, 2015. [PubMed: 26087111]

9. Hosseini SM, Wilson W, Ito K and, van Donkelaar CC. How preconditioning affects the measurement of poro-viscoelastic mechanical properties in biological tissues. Biomech. Model. Mechanobiol. 13:503–513, 2014. [PubMed: 23864393]

10. Humphrey JD, Vawter DL and, Vito RP. Quantification of strains in biaxially tested soft tissues. J. Biomech. 20:59–65, 1987. [PubMed: 3558429]

11. Jett SV, Hudson LT, Baumwart R, Bohnstedt BN, Mir A, Burkhart HM, Holzapfel GA, Wu Y and, Lee C-H. Integration of polarized spatial frequency domain imaging (pSFDI) with a biaxial mechanical testing system for quantification of load-dependent collagen architecture in soft collagenous tissues. Acta Biomater. 2019 (in press), 10.1016/j.actbio.2019.11.028.

12. Jimenez JH, Soerensen DD, He Z, He S and, Yoganathan AP. Effects of a saddle shaped annulus on mitral valve function and chordal force distribution: An in vitro study. Ann. Biomed. Eng. 31:1171–1181, 2003. [PubMed: 14649491]

13. Khoiy KA and, Amini R. On the biaxial mechanical response of porcine tricuspid valve leaflets. J. Biomech. Eng. 138:104504, 2016.

14. Klabunde R Cardiovascular Physiology Concepts. Lippincott Williams & Wilkins, 2011.

15. Lam JHC, Ranganathan N, Wigle ED and, Silver MD. Morphology of the human mitral valve. Circulation 41:449–458, 1970. [PubMed: 5415982]

16. Lee C-H, Rabbah J-P, Yoganathan AP, Gorman RC, Gorman JH III and, Sacks MS. On the effects of leaflet microstructure and constitutive model on the closing behavior of the mitral valve. Biomech. Model. Mechanobiol. 14:1281–1302, 2015. [PubMed: 25947879]

17. Liao J and, Vesely I. A structural basis for the size-related mechanical properties of mitral valve chordae tendineae. J. Biomech. 36:1125–1133, 2003. [PubMed: 12831738]

18. Lomholt M, Nielsen SL, Hansen S, Andersen NT and, Hasenkam JM. Differential tension between secondary and primary mitral chordae in an acute in-vivo porcine model. J. Heart Valve Dis. 11:337–345, 2002. [PubMed: 12056724]

19. Ogden R Elastic deformations of rubberlike solids. In: Mechanics of Solids, Elsevier, 1982, pp. 499–537.

20. Phillips MR, Daly RC, Schaff HV, Dearani JA, Mullany CJ and, Orszulak TA. Repair of anterior leaflet mitral valve prolapse: Chordal replacement versus chordal shortening. Ann. Thorac. Surg. 69:25–29, 2000. [PubMed: 10654480]

21. Pokutta-Paskaleva A, Sulejmani F, DelRocini M and, Sun W. Comparative mechanical, morphological, and microstructural characterization of porcine mitral and tricuspid leaflets and chordae tendineae. Acta Biomater. 85:241–252, 2019. [PubMed: 30579963]

22. Prot V, Skallerud B, Sommer G and, Holzapfel GA. On modelling and analysis of healthy and pathological human mitral valves: Two case studies. J. Mech. Behav. Biomed. Mater. 3:167–177, 2010. [PubMed: 20129416]

23. Rabbah J-P, Saikrishnan N and, Yoganathan AP. A novel left heart simulator for the multi-modality characterization of native mitral valve geometry and fluid mechanics. Ann. Biomed. Eng. 41:305–315, 2013. [PubMed: 22965640]

24. Ritchie J, Jimenez J, He Z, Sacks MS and, Yoganathan AP. The material properties of the native porcine mitral valve chordae tendineae: An *in vitro* investigation. J. Biomech. 39:1129–1135, 2006. [PubMed: 16549101]

25. Sedransk KL, Grande-Allen KJ and, Vesely I. Failure mechanics of mitral valve chordae tendineae. J. Heart Valve Dis. 11:644–650, 2002. [PubMed: 12358400]

26. Shah PM Current concepts in mitral valve prolapse—Diagnosis and management. J. Cardiol. 56:125–133, 2010. [PubMed: 20702064]

27. Silver MD, Lam JHC, Ranganathan N and, Wigle ED. Morphology of the human tricuspid valve. Circulation 43:333–348, 1971. [PubMed: 5544987]

28. Smedira NG, Selman R, Cosgrove DM, McCarthy PM, Lytle BW, Taylor PC, Apperson-Hansen C, Stewart RW and, Loop FD. Repair of anterior leaflet prolapse: Chordal transfer is superior to chordal shortening. J. Thorac. Cardiovasc. Surg. 112:287–292, 1996. [PubMed: 8751492]

29. Sousa UM, Grare P, Jebara V, Fuzelier JF, Portoghese M, Acar C, Relland J, Mihaileanu S, Fabiani JN and, Carpentier A. Transposition of chordae in mitral valve repair. Mid-term results. Circulation 88:II35–38, 1993. [PubMed: 8222177]

30. Stemper BD, Yoganandan N, Stineman MR, Gennarelli TA, Baisden JL and, Pintar FA. Mechanics of fresh, refrigerated, and frozen arterial tissue. J. Surg. Res. 139:236–242, 2007. [PubMed: 17303171]

31. Storn R and, Price K. Differential evolution–A simple and efficient heuristic for global optimization over continuous spaces. J. Global Opt.W 11:341–359, 1997.

32. Tabata M, Kasegawa H, Fukui T, Shimizu A, Sato Y and, Takanashi S. Long-term outcomes of artificial chordal replacement with tourniquet technique in mitral valve repair: A single-center experience of 700 cases. J. Thorac. Cardiovasc. Surg. 148:2033–2038.e2031, 2014. [PubMed: 24768103]

33. Waller BF, Howard J and, Fess S. Pathology of tricuspid valve stenosis and pure tricuspid regurgitation—Part I. Clin. Cardiol. 18:97–102, 1995. [PubMed: 7720297]

34. Zuo K, Pham T, Li K, Martin C, He Z and, Sun W. Characterization of biomechanical properties of aged human and ovine mitral valve chordae tendineae. J. Mech. Behav. Biomed. Mater. 62:607–618, 2016. [PubMed: 27315372]
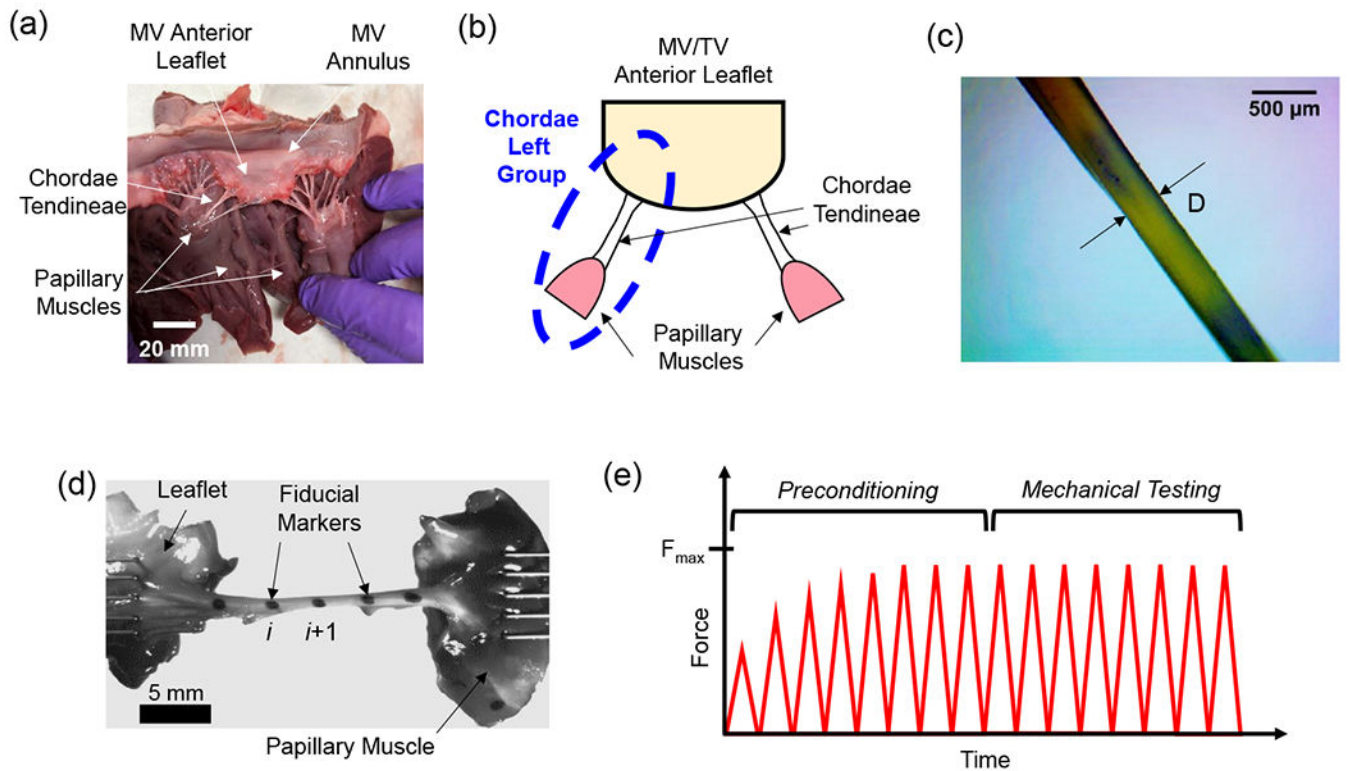
Figure 1 –.
(a) Photo of a dissected representative porcine atrioventricular heart valve (MV). (b) Schematic of the leaflet-strut CT-papillary muscle entities from the left side and the right side of the leaflet's apex. (c) Measurement of the chordae thickness (D) by a microscope. (d) Experimental setting of the leaflet-CT-PM entity using the tined BioRakes. (e) Uniaxial mechanical testing protocol for characterizing the leaflet-CT-PM tissue entities (the targeted target force: F_{max} = 1.4 N for the MVAL strut CT tissues, and F_{max} = 1.2 N for the TVAL strut CT tissues).
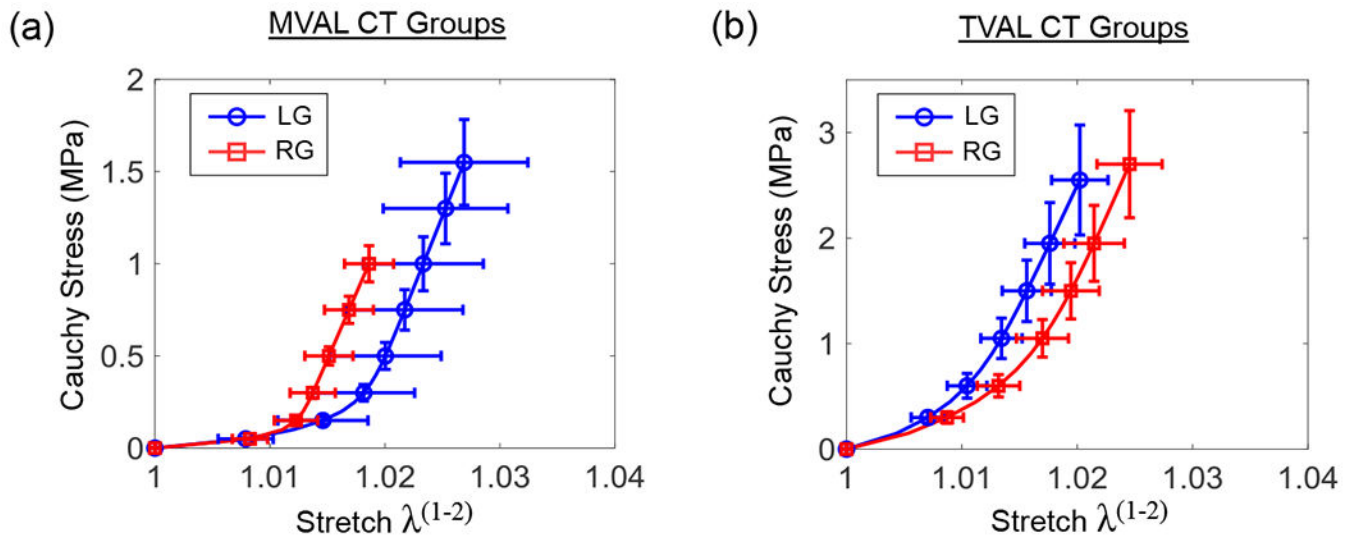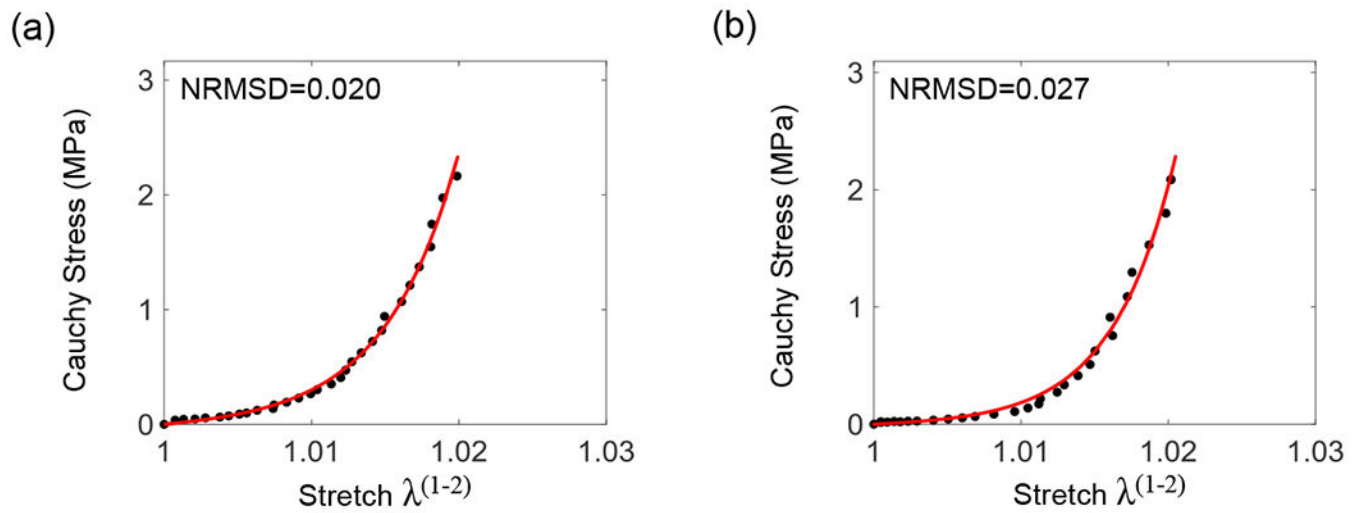
Figure 2 –.
Cauchy stress versus stretch responses of (a) the MVAL strut CT, and (b) the TVAL strut CT.
Values are reported as mean ± SEM (n=12).

(a)

(b)

(c)

(d)
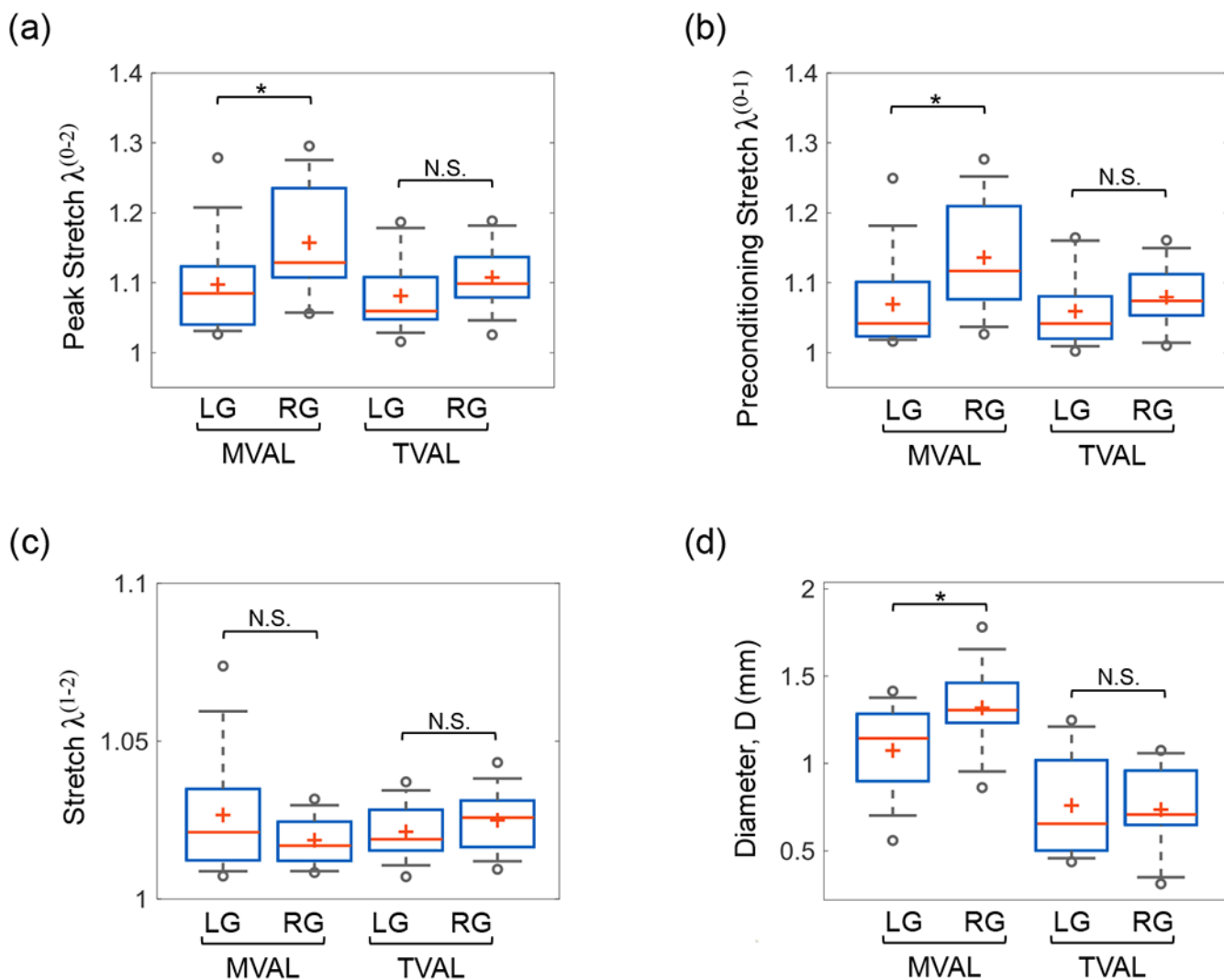
Figure 3 –.
Box plots of (a) peak stretch, (b) preconditioning stretch, (c) stretch, and (d) diameter *D* of the MVAL and TVAL strut CT tissues. * denotes statistically significant difference (p<0.05) and N.S. denotes not statistically significant.

(a)

(b)

Figure 4 –.
Representative Ogden model fits to the Cauchy stress-stretch data: (a) MVAL-LG #5 ($\mu =$ 40.8 kPa; $\alpha = 205.2$), and (b) TVAL-LG #1 ($\mu = 17.7$ kPa; $\alpha = 241.2$). (black dots (•) denote experimental data, and red solid curves (–) refer to the Ogden constitutive model fits).
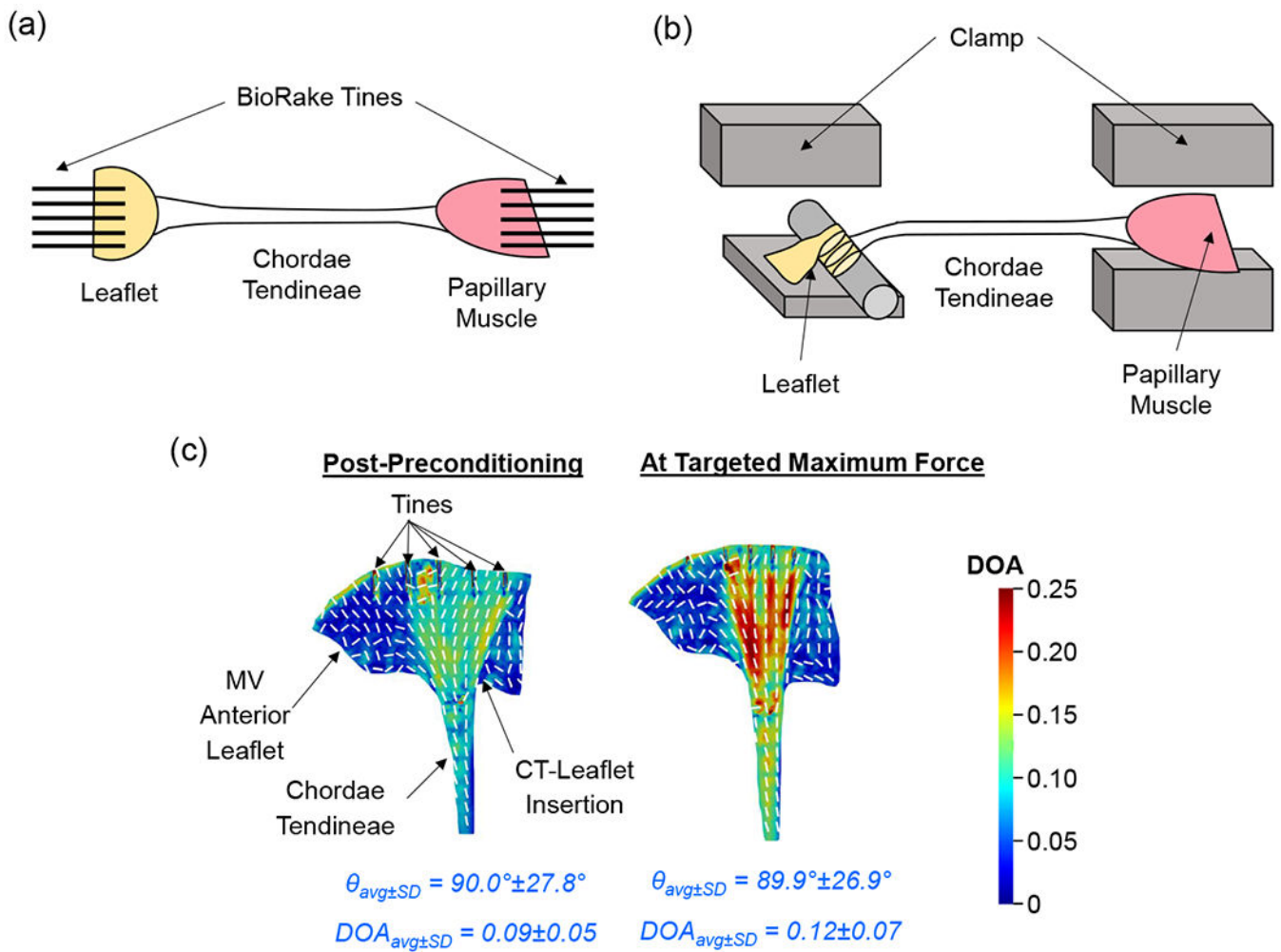
Figure 5 –.
(a) Schematic of the uniaxial testing setup of the present study, which allows the analysis of tissue deformation of strut chordae tendineae, especially for the chordae-leaflet insertion and the chordae-PM attachment. (b) Comparison to the clamp-based testing configuration used in the previous study.[8] (c) Preliminary findings of the collagen fiber orientation θ and the degree of optical anisotropy (DOA) of the MVAL chordae-leaflet insertion region at the post-preconditioned state and at the maximum force loading state.
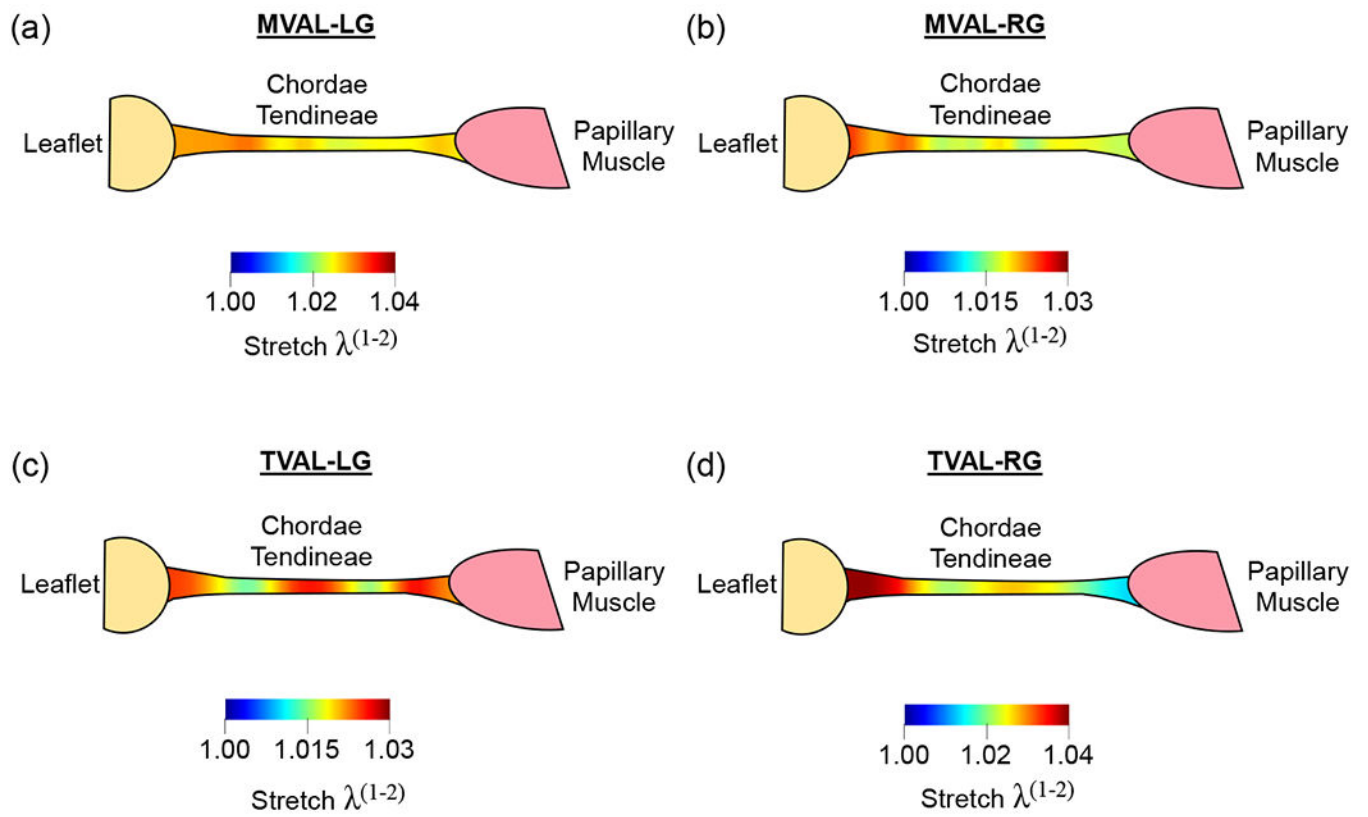
Figure 6 –.
Distributions of the stretch across the CT domain determined by the cubic B-spline fitting (n=12): (a) MVAL-LG, (b) MVAL-RG, (c) TVAL-LG, and (d) TVAL-RG.
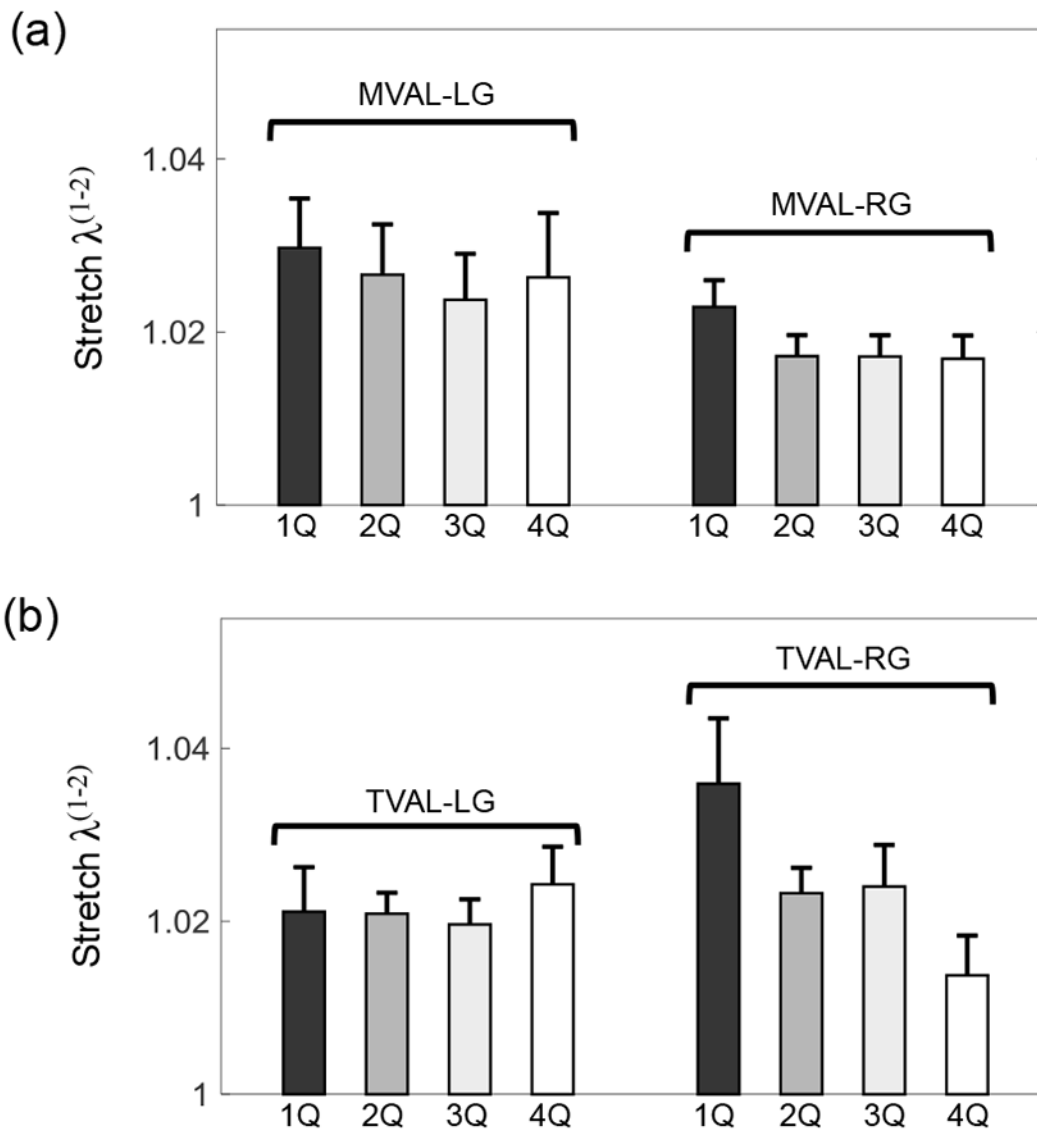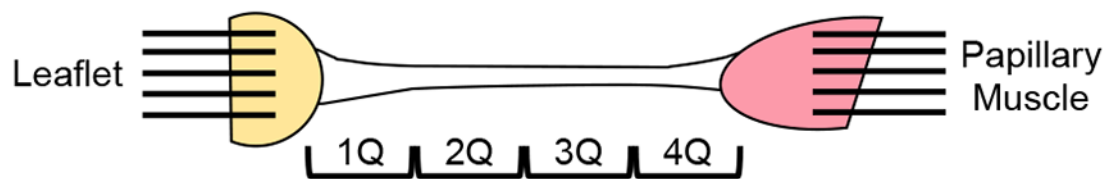
Figure 7 –.
Variations in the stretch of the four quarter-sections of the CT segment: (a) MVAL strut chordae, and (b) TVAL strut chordae. Values are reported as mean ± SEM (n=12)

Table 1 –

Estimated Ogden model parameters for the strut CT, together with comparisons to other studies in the literature. (NRMSD: normalized root-mean-square deviation)

ID	MVAL-LG			MVAL-RG			TVAL-LG			TVAL-RG		
	μ (kPa)	a	NRMSD	μ (kPa)	a	NRMSD	μ (kPa)	a	NRMSD	μ (kPa)	a	NRMSD
1	581.8	217.5	0.029	2.1	267.8	0.042	17.1	241.2	0.027	159.4	90.3	0.039
2	8.7	221.5	0.019	63.4	212.1	0.052	698.0	130.8	0.028	188.3	86.1	0.022
3	27.8	220.7	0.017	5.9	331.6	0.027	174.7	146.9	0.043	16.6	172.6	0.039
4	1.5	193.7	0.028	4.2	239.6	0.016	764.9	101.3	0.042	72.6	110.0	0.051
5	40.8	205.2	0.020	13.3	407.6	0.043	1321.7	158.1	0.153	3797.4	107.6	0.046
6	4.6	87.5	0.015	88.6	302.7	0.034	1104.1	142.8	0.028	291.2	152.3	0.030
7	13.0	130.1	0.024	10.7	257.8	0.023	63.3	163.2	0.042	77.3	210.8	0.069
8	0.2	179.8	0.017	36.3	271.3	0.023	129.7	113.6	0.029	146.7	94.9	0.023
9	66.4	206.6	0.029	127.0	294.1	0.039	936.2	55.4	0.044	82.0	106.2	0.032
10	79.6	160.6	0.022	1.5	221.0	0.029	250.8	121.1	0.046	180.9	69.7	0.035
11	143.9	288.3	0.084	5.6	213.2	0.034	449.1	113.7	0.071	140.9	255.5	0.106
12	65.9	295.5	0.049	0.4	236.6	0.024	27.6	105.7	0.051	333.2	161.6	0.094
Mean	86.2	200.6	–	29.9	271.3	–	494.8	132.8	–	457.2	134.8	–
SEM	46.7	16.9	–	12.0	16.4	–	131.8	13.0	–	304.8	16.3	–

Other studies in the literature	μ (kPa)	a
Porcine MVAL Struct CT (n=20) Pokutta-Paskaleva et al. (2019)	20.0	65.3
Porcine TVAL Struct CT (n=18) Pokutta-Paskaleva et al. (2019)	150.0	86.5
Ovine MVAL Struct CT (n=18) Zuo et al. (2016)	0.9±2.7	28.0±27.1

Table 2 –

Comparison of tissue stretches and Cauchy stresses between the present study of chordae tendineae and the previous literature on testing individual chordae segments. Values are reported as either mean ± standard error of the mean (SEM) or mean ± standard deviation (SD), as indicated.

Study (Species)	MVAL Strut CT (n=12)		TVAL Strut CT (n=12)	
	$\lambda^{(1-2)}$ (-)	Cauchy Stress (MPa)	$\lambda^{(1-2)}$ (-)	Cauchy Stress (MPa)
Present Work (Porcine)	LG: 1.03±0.01 RG: 1.02±0.01 (mean ± SEM)	LG: 1.59±0.16 RG: 1.04±0.08 (mean ± SEM)	LG: 1.02±0.01 RG: 1.03±0.01 (mean ± SEM)	LG: 2.71±0.10 RG: 2.89±0.01 (mean ± SEM)
Pokutta-Paskaleva et al. (2019) (Porcine, MVAL, n=20; TVAL, n=18)	1.09 *	3.50	1.037	3.35
Ritchie et al. (2006) (Porcine, n = not provided)	1.05	0.89 to 1.18	–	–
Liao and Vesely (2003) (Porcine, n=16)	1.16±0.03 (mean ± SD)	11.24	–	–
Zuo et al. (2016) (Ovine, n=18)	1.07±0.08 [1.02±0.08] (mean ± SD)	24.00 [1.20]	–	–
Prot et al. (2010) (Human, n=1)	1.06 [1.05]	3.00 [1.50]	–	–

*Stretch and stress values are associated with the peak loading for each study.

†Values in the square brackets are data in the Cauchy stress range comparable to the present study.